

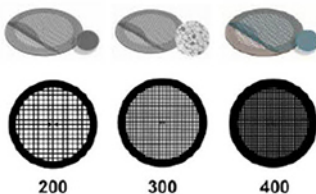
Nanocharacterization by TEM and AFM

We offer a wide range of TEM and AFM tools, from TEM grids and finders to AFM substrates and grippers.

Available in a wide variety of designs and materials to support your work, select from a broad range of mesh sizes, specimen supporting films, and materials that perfectly suit the conditions of your TEM analysis.

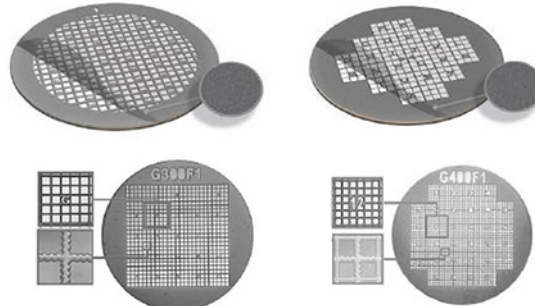
TEM grid specifications:

Material	Mesh Size and Shape	Film Specifications
<ul style="list-style-type: none">• Cu• Ni• Au• Mo• Cu/Pd	<ul style="list-style-type: none">• Square or hexagonal• Single-hole grid (75 mm or 100 mm)• 100• 150• 200• 300• 400	<ul style="list-style-type: none">• None• Continuous formvar film (thicknesses: 5-6 nm, 10 nm)• Lacey carbon film (average hole sizes: 50 nm, 100 nm, 150 nm, 100 nm, 150 nm)• Continuous amorphous carbon film (thicknesses: 10 nm, 20-30 nm)• Continuous formvar/carbon film (thickness: 10nm formvar and 1nm carbon)



TEM finder grid specifications:

Material	Mesh Size	Film Specifications
<ul style="list-style-type: none">• Cu• Ni• Au	<ul style="list-style-type: none">• 135• 200• 300• 400	<ul style="list-style-type: none">• None• Continuous amorphous carbon film (thicknesses: 3-4 nm, 10 nm, 20-30 nm)



Supporting Tools for Nanomaterial Characterization

Our comprehensive range of supporting materials for nanomaterial characterization includes tweezers (sharp tip, disc gripper for AFM), TEM window grids (various thicknesses, 1 or 9 windows), a magnetic pick-up tool, a grid storage box, cryo-capsules, lift-out grids (Cu or Mo), AFM substrates (various dimensions), and much more.



Explore our complete range of TEM grids on:
[SigmaAldrich.com/nanocharacterization](https://www.sigmaaldrich.com/nanocharacterization)

© 2022 Merck KGaA, Darmstadt, Germany and/or its affiliates. All Rights Reserved. Merck, the vibrant M, and Sigma-Aldrich are trademarks of Merck KGaA, Darmstadt, Germany or its affiliates. All other trademarks are the property of their respective owners. Detailed information on trademarks is available via publicly accessible resources.

MK_AD9792EN 43729 08/2022

The Life Science business of Merck operates as MilliporeSigma in the U.S. and Canada.

Sigma-Aldrich®
Lab & Production Materials

(Near-) Infrared Drying of Lithium-Ion Battery Electrodes: Influence of Energy Input on Process Speed and Electrode Adhesion

Andreas Altvater,* Thilo Heckmann, Jochen Christoph Eser, Sandro Spiegel, Philip Scharfer, and Wilhelm Schabel

The drying of electrodes represents a critical process step in the production of lithium-ion batteries. In this process step, unfavorably adjusted drying conditions can result in deteriorated electrode properties. Furthermore, the process speed is restricted by limited heat and mass transfer in purely convective drying. To counteract those effects, energy input by near-infrared (NIR) radiation is a promising approach. Herein, analytical considerations are carried out to demonstrate the suitability of infrared radiation with regard to achievable electrode temperatures and drying rates. In an experimental approach, aqueous processed graphite anodes are dried with an NIR module, varying the power and the amount of convection for different experiments. The temperature profiles of the electrodes and the drying rates are measured and analyzed, and the electrodes are subsequently characterized using adhesion measurements. The results obtained show that energy input by NIR radiation during the drying of electrodes can lead to an increased drying speed, electrode temperature during drying, and adhesion force of the dry electrode. These findings indicate that the binder distribution during NIR drying is advantageous in terms of electrode adhesion, compared with convectively dried electrodes produced at comparable drying rates, positioning the process promisingly with regard to high throughput rates.

energy demand on the one hand and drying condition-dependent electrode properties on the other demand the necessity of an optimally conducted drying process.^[3,4] The negative influence on the product properties thereby primarily occurs at high drying rates.^[5] The application of high drying rates can lead to a migration of additives like binder and carbon black to the surface of the electrode layer, resulting in low adhesion between active material and current collector foil.^[6–10] Furthermore, the electrochemical performance deteriorates compared with gently dried electrodes due to the accumulation of insulating binder and carbon black at the surface, resulting in an increased electrical resistance.^[6,11]

Binder migration is attributed to the capillary pressure-driven induction of concentration differences during the emptying of the porous electrode structure, leading to an inhomogeneous distribution of components over the electrode height.^[5]

Nevertheless, it has been shown that these effects can be compensated for by selecting suitable process parameters. Isothermal drying tests indicate that a high film temperature and a low heat transfer coefficient can have a positive effect on adhesion, therefore indicating a more homogeneous distribution of electrode components.^[9]

The authors reasoned that binder diffusion processes could take place to compensate for concentration differences caused by capillary pore emptying to some extent. Due to the proportionality of diffusion coefficient and temperature, as well as the antiproportionality of viscosity and temperature, higher electrode temperatures increase binder mobility and therefore adhesion.^[6,9,11]

In addition, the authors illustrate the influences and limitations regarding electrode temperature and drying rate in the convective drying process, which are determined by air temperature, convective heat transfer coefficient, and humidity. Based on an enthalpy balance for double-sided heat input, a maximum electrode temperature of about 50 °C is determined during the evaporation process, while the air temperature was set to 150 °C, the dew point to 15 °C, and the convective heat transfer coefficient to 80 W m⁻² K⁻¹, resulting in a drying rate of 6.15 g m⁻² s⁻¹.^[9]

These limitations in terms of electrode film temperature are due to the enthalpy transferred with the evaporation flow, which cools the electrode layer below the temperature of the supplied air.

1. Introduction

The drying of electrodes is a crucial and often limiting process step in the manufacturing chain of lithium-ion batteries.^[1] While the coating step can be carried out at high coating speeds, as shown by Diehm et al., the application of high drying rates still challenges the throughput in electrode production.^[2] High

A. Altvater, T. Heckmann, J. C. Eser, S. Spiegel, P. Scharfer, W. Schabel
Material Research Center for Energy Systems (MZE)
Thin Film Technology (TFT)
Karlsruhe Institute of Technology (KIT)
76131 Karlsruhe, Germany
E-mail: andreas.altvater@kit.edu

 The ORCID identification number(s) for the author(s) of this article can be found under <https://doi.org/10.1002/ente.202200785>.

© 2022 The Authors. Energy Technology published by Wiley-VCH GmbH. This is an open access article under the terms of the Creative Commons Attribution-NonCommercial-NoDerivs License, which permits use and distribution in any medium, provided the original work is properly cited, the use is non-commercial and no modifications or adaptations are made.

DOI: 10.1002/ente.202200785

Due to the facts listed earlier, one promising approach to achieve higher film temperatures in the process is the application of heat input by radiation. Compared with convective drying, the heat and mass transfer are to a certain extent decoupled from each other in radiation-assisted drying. In this way, the energy input can be controlled without significantly affecting the mass transfer coefficient, enabling higher electrode temperatures at comparable drying rates.

Although heat input by infrared radiation is widely used, for instance, in the food and paper industry, there is not yet a sufficient knowledge base for the application in battery electrode drying.^[12] Nevertheless, initial work on the radiation-based drying of electrodes is available in literature.^[13–17] Vedder et al. showed first results of first-cycle coulombic efficiency of half cells and adhesion of electrodes. The authors found no dependence of electrochemical functionality and morphology on the drying method for graphite-based anodes when comparing drying with a fiber laser at a wavelength of 1070 nm with convective oven drying, while reducing energy consumption by a factor of 2.^[13] Günther et al. investigated a drying process inducing different stages of resulting film temperatures by means of IR radiation. They showed that rapid drying with a large-area infrared dryer can lead to separation of the active particles and the binder, which affects the adhesion and cohesion strength of the dried electrode.^[17] For spinel-type LiMn₂O₄ cathodes, Kim et al. found that the NIR drying process reduces required drying time and provides longer lifetime of the batteries.^[15] Wu et al. investigated the influence of process parameters on residual moisture content and drying rate in convective and infrared drying of LiCoO₂ cathodes and concluded that the drying efficiency is higher in infrared drying. However, the authors found that, for the specific processes investigated, the energy utilization rate in a certain drying stage in infrared drying is lower than in convective drying.^[14] Wiegmann et al. produced graphite anodes with reduced solvent content in an IR drying process and found a correlation between the applied area-related intensity and the electrode properties. With increasing intensity up to a certain limit, a slight increase in adhesion strength was observed while the standard deviation decreased. At intensities above the limit, lower adhesion and increasing standard deviation were observed. The initial increase in adhesion was explained by the softening of the binder due to the increasing heat generation, which causes a change in the microstructure of the binder. The following decrease in adhesion was explained by the dissipation of binder clusters due to excessive heat input.^[18]

To deepen these initial investigations, systematic studies on the influence of the adjusted infrared power as well as the convection component on the electrode temperature and drying rate for the drying of water-based graphite anodes are presented in this work. Following calculations which underline the suitability of the infrared process, experimental investigations are shown and discussed. To clearly identify the differences in process influences, three process variants were investigated: pure convection drying, infrared drying in combination with forced convection, and pure infrared drying. The process data of all variants was analyzed and evaluated with respect to an influence on the resulting electrode structure in terms of binder distribution, indirectly quantified by adhesive force measurements.

2. Calculated Electrode Film Temperature and Drying Rate in the First Drying Section

In drying applications, the process can be described by an enthalpy balance of the drying film. For the example of electrode drying with heat input by convection or radiation, the basic correlation is shown in Equation (1).

$$\frac{dh_{\text{El}}}{dt} = \frac{d(m_{\text{El}}c_{p,\text{El}}T_{\text{El}})}{dt} = \dot{q}_{\text{Convection}} + \dot{q}_{\text{Radiation}} - \dot{h}_{\text{S}} \quad (1)$$

In this equation, the time-dependent change of the film enthalpy is represented by $\frac{dh_{\text{El}}}{dt}$, the area-related electrode mass by m_{El} , its heat capacity by $c_{p,\text{El}}$, and its temperature at the respective time by T_{El} . The factors that determine the enthalpy change are the heat input by convection ($\dot{q}_{\text{Convection}}$) and radiation ($\dot{q}_{\text{Radiation}}$) as well as the enthalpy flow of the evaporating solvent (\dot{h}_{S}). In order to calculate the enthalpy of the electrode h_{El} , all of the components of the drying electrode, including solvent and current collector, have to be considered. For reasons of scalability, the enthalpy of the electrode, as well as the heat fluxes and the enthalpy flow due to evaporation are related to the relevant electrode area A_{El} .

The heat inputs listed in Equation (1) depend on the process parameters. In the case of convective heat flux, the temperature gradient between the drying film and the surrounding air T_{∞} and the heat transfer coefficient α , resulting from the air flow conditions and nozzle design is decisive, as shown in Equation (2).

$$\dot{q}_{\text{Convection}} = K_A \alpha (T_{\infty} - T_{\text{El}}) \quad (2)$$

The Ackermann correction factor K_A considers enthalpy flows due to evaporation which influence the heat transfer.

In the case of heat input by radiation, the emissivity of the material ε in combination with the emitted wavelength λ and power of the radiation source is relevant. Here, the mass transfer is not conducted by forced but by free convection. Therefore, the heat transfer coefficient is calculated by the correlations listed in VDI Heat Atlas, Chapter F2, Section 3.^[19]

The parameters used as a basis here can be further subdivided in directly adjustable process parameters like flow velocity of the drying air or distance and emission angle of the radiation module. In order to enable a consideration which is independent of dryer geometries and individual process modules, exclusively generally applicable, area-related parameters such as the heat transfer coefficient α and the heat input through radiation $\dot{q}_{\text{Radiation}}$ are used.

The outgoing enthalpy flow depends on the mass flow of the evaporating solvent \dot{m}_{S} , which corresponds to the drying rate (compare Equation (3)).

$$\dot{h}_{\text{S}} = \dot{m}_{\text{S}} \Delta h_{\text{v}}(T_{\text{El}}) = \tilde{M}_{\text{S}} \tilde{\rho}_{\text{G}} \beta_{\text{S,G}} \ln \left(\frac{1 - \tilde{y}_{\text{S},\infty}}{1 - \tilde{y}_{\text{S,Ph}}} \right) \Delta h_{\text{v}}(T_{\text{El}}) \quad (3)$$

The drying rate depends on the molar mass of the solvent \tilde{M}_{S} , the molar density of the gas phase $\tilde{\rho}_{\text{G}}$, the mass transfer coefficient $\beta_{\text{S,G}}$, as well as the molar fractions of the solvent in the surrounding gas phase $\tilde{y}_{\text{S},\infty}$ and at the phase boundary of the electrode $\tilde{y}_{\text{S,Ph}}$. $\Delta h_{\text{v}}(T_{\text{El}})$ represents the enthalpy of evaporation

at the prevailing film temperature. To describe the mass transfer coefficient, the Lewis analogy is used.^[19] The molar fractions depend on the dew-point temperature in the gas phase and the electrode temperature via the vapor pressure. The vapor pressure at the respective temperature is calculated using a Wagner equation and applied to Equation (4).^[9,19]

$$\tilde{y}_{S,\infty} = \frac{p^*(T_{Dew})}{p_\infty} \text{ and } \tilde{y}_{S,Ph} = \frac{p^*(T_{El})}{p_\infty} \quad (4)$$

Here, $p^*(T)$ represents the saturated vapor pressure at a given temperature, while p_∞ is the environmental pressure. A list of the boundary conditions, material data, equations, and correlations used can be found in the Supporting Information.

In the drying process of capillary porous goods, such as wet-coated electrodes, a steady state usually develops after an initial heating-up phase for the case of constant process parameters. In this first drying section, which is called constant rate period, the incoming and outgoing enthalpy flows coincide, resulting in a constant temperature T_{Steady} of the drying layer on the one hand and a constant drying rate on the other.^[20] The described stationary temperature corresponds to the wet bulb temperature which is frequently referred to in drying literature. As Kumberg et al. showed that electrodes up to a certain thickness primarily dry in the first drying section, this section is considered to be predominant throughout this work.^[21] To illustrate the processes in the first drying section, the temperature profiles and the profiles of the water fraction in the drying electrode film and in the boundary layer above the film are shown qualitatively in **Figure 1** for various cases. In addition, the incoming and outgoing heat and enthalpy flows are indicated.

Figure 1a shows the example of purely convective drying. Here, the film temperature is always lower than the air temperature, due to the escaping enthalpy flow caused by evaporation which is particularly high in the case of the solvent water due to the immense enthalpy of evaporation. The second illustration (Figure 1b) represents drying with a combination of heat input by radiation and application of forced convection, in which the air temperature in the dryer is adjusted to match the electrode film temperature. The last scheme (Figure 1c) shows drying where

the heat input is only realized by radiation. In this way, film temperatures are achieved that are significantly higher than the ambient air temperature. Hereby, the mass transfer in the gas phase is dominated by a free convection flow, which arises due to the resulting temperature and density gradients. A detailed explanation will follow later.

As the parameters steady-state temperature and drying rate in the first drying section are decisive for structure formation and electrode properties, they are quantitatively determined for different parameter settings for the cases “forced convection” and “radiation and free convection,” which are essentially different with regard to the type of energy input. The process data of interest can thus be calculated under the assumption of a one-sided, adiabatic, that is energy-loss-free, drying process. To provide a basic overview, possible influences of specific dryer designs, such as radiant heat from dryer hood surfaces, are not considered for the time being. Furthermore, in the first drying stage, it is sufficient to only consider the solvent, as the mass and temperature of the solid components in Equation (1) do not change. The parameters varied are the convective heat transfer coefficient, the temperature of the drying air T_∞ , the dew point temperature of the drying air T_{Dew} , and the heat flux by radiation $\dot{q}_{Radiation}$. For different combinations of these parameters, the results are depicted in **Figure 2**.

The diagram in Figure 2a shows the drying rate and the temperature for different scenarios in the purely convective drying process. The data describing a drying process with a convective heat transfer coefficient of $30 \text{ W m}^{-2} \text{ K}^{-1}$ and a dew point of the drying air of 5°C shows a relatively moderate drying rate that can be increased by raising the air temperature. The same applies to the steady-state temperature, which, however, does not exceed a value of $\approx 40^\circ \text{C}$, even for high air temperatures of 150°C . In addition to increasing the temperature of the drying air, the steady-state temperature can be increased by raising the dew point, that is, the relative humidity. An increase of the dew point to 50°C with the same heat transfer coefficient leads to significantly higher steady-state temperatures of $\approx 60^\circ \text{C}$. However, the drying rate is significantly reduced due to the decreasing gradient of the molar fractions of the solvent in the gas phase (compare Equation (3)). Another possibility for process control is to increase the convective heat transfer coefficient. In this case,

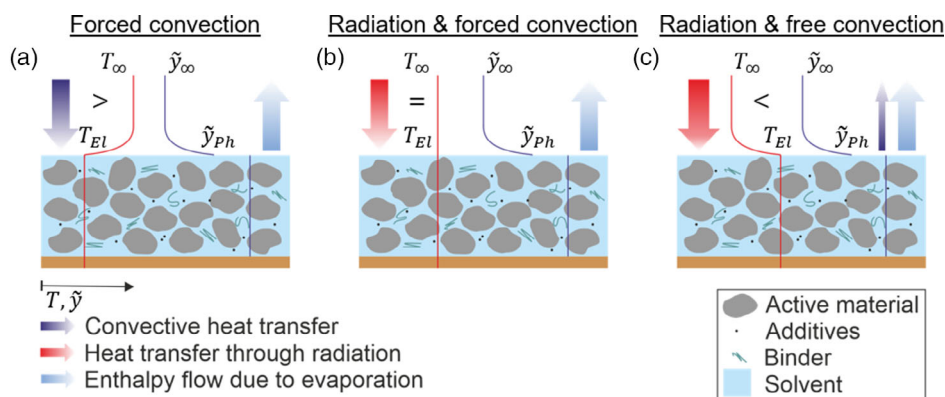


Figure 1. Schematic illustration of the temperature and solvent molar fraction profiles and heat and enthalpy flows during the drying of battery electrodes with different drying settings. a) Purely convective drying; b) convective drying with heat input by infrared radiation, while the air temperature was set to correspond to the electrode film temperature; c) drying solely by heat input using infrared radiation. Gradients in the film as well as heat transfer processes on the bottom side of the electrode are neglected in this figure.

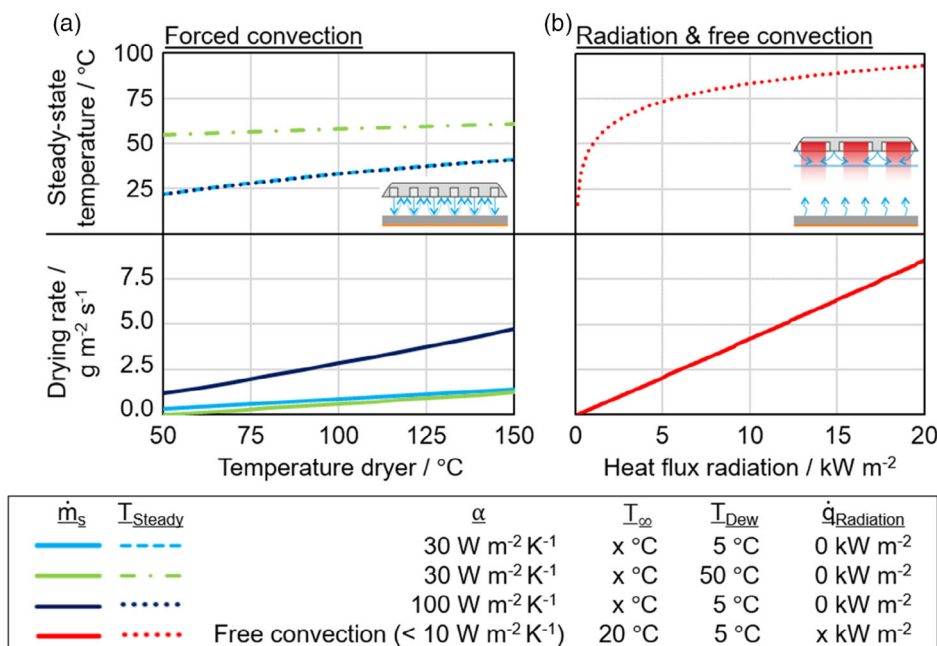


Figure 2. Analytical calculations of the drying rate and steady-state temperature during drying of aqueous graphite anodes as a function of the applied drying air temperature in a) convective drying and the b) applied area-related heat flux through radiation for different parameter settings. The integrated schematic drawings refer to the drying technology used.

high drying rates can be achieved, but only comparatively low electrode temperatures can be reached.

The diagram on the right (Figure 2b) shows the drying rate and temperature for a drying process that is carried out with heat input by radiation and surrounding air at 20 °C with a dew point temperature of 5 °C. With increasing heat input by radiation, the drying rate and the steady-state temperature increase. The steady-state temperature rises sharply at the beginning with slight increases in power, after which the temperature curve asymptotically approaches the boiling temperature of water with further increases in power. The drying rate curve indicates an almost linear increase with increasing power input.

The comparison of the two drying processes essentially makes one key statement: Comparable or higher drying rates can be achieved with heat input by radiation as with convective drying. However, the achievable steady-state temperature of the drying electrode film is significantly higher with purely radiation-induced heat input, which underscores the suitability of the process for drying electrodes at high drying rates with acceptable electrode properties. The higher temperatures at comparable drying rates are primarily due to the absence of forced convection, which is responsible for heat and mass transfer in the purely convective drying process. In the case of purely radiation-driven drying, the temperature difference between the boundary layer above the drying electrode layer and the ambient air results in a free convection flow with a heat transfer coefficient α_{FC} , which is significantly lower ($<10 \text{ W m}^{-2} \text{ K}^{-1}$) than in drying processes with forced convection (compare Figure 1c). This, in combination with the approximately logarithmic relationship between film temperature and drying rate (compare Equation (3) and (4)), leads to the positive combination of high film temperatures and high drying rates in the radiation-based drying process.

3. Drying Curves: Electrode Film Temperature and Solvent Evaporation

Drying experiments were conducted with water-based anode slurries, consisting of graphite, carbon black, and the binder system carboxymethyl cellulose (CMC) and styrene-butadiene-rubber (SBR). The drying process for different process variants was evaluated by means of mass and temperature curves while the dried electrodes were characterized by adhesion tests.

To this end, the influence of adjusted power of the infrared module and convection of drying air on the drying of aqueous-processed anodes was evaluated on a laboratory scale. The process variations “forced convection,” “radiation and forced convection,” and “radiation and free convection” were investigated.

3.1. Forced Convection

In Figure 3, the solvent loading and temperature curves for the process variant “forced convection” are shown for two settings of the temperature of the drying air. The lower half of the graph shows the solvent loading in mass of solvent per mass of dry electrode over time. Data points each correspond to a single measurement value of the scale. The upper half of the diagram shows the temperature curve based on the data recorded with a thermocouple attached to the underside of the current collector.

The drying curves show similar profiles for both settings but differ quantitatively. In both cases the electrode temperature initially rises to a higher value than the coating temperature prior to drying. Following this heating phase, a constant temperature is established, which is maintained for a certain period of time. This represents the constant rate period (compare Section 2),

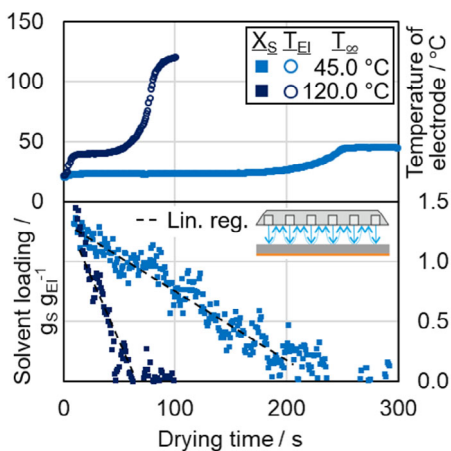


Figure 3. Solvent loading and temperature profiles of electrodes during drying of aqueous-processed anodes: process variant “forced convection” with variation of the drying air temperature with an initial dew point of 8.9 °C and a mean convective heat transfer coefficient of 80.0 W m⁻² K⁻¹.

in which both temperature and evaporation rate remain constant. At the end of this period, the temperature rises and approaches the drying air temperature, indicating that the film has completely dried. In comparison, the course of the solvent loading X_S shows fluctuations, which are caused by the impulse of the convection flow on the balance. Nevertheless, the data in both cases show in average a linear decrease of the solvent loading in the steady state and can be analyzed especially with regard to the resulting drying rate. It is noticeable that the decrease in solvent loading with time is clearly steeper at the higher temperature. Both values increase for the higher temperature setting, which can be explained by the higher temperature gradient with increasing drying air temperature. The gradient determines the enthalpy introduced, resulting in a higher film temperature, which again leads to a higher drying rate due to the temperature-dependent water vapor pressure and therefore the higher molar

Table 1. Overview of the set parameters and process data for the three process variants.

Process variant	Process parameters			Experimental data	
	T_∞ [°C]	α [W m ⁻² K ⁻¹]	$p_{el, IR}$ [kW m ⁻²]	\dot{m}_S [g m ⁻² s ⁻¹]	T_{Steady} [°C]
Forced convection	45.0	80.0 ^{a)}	0.0	0.81	23.1
	120.0			2.80	31.8
IR + forced convection	21.3	36.5 ^{a)}	12.2	0.75	31.1
			29.3	2.05	49.2
			48.9	5.54	60.8
IR + free convection	21.3	6.0 ^{b)}	12.2	0.60	51.4
			29.3	2.54	74.6
			48.9	6.08	81.1

^{a)}Characterized by means of measurements using thermochromic liquid crystals (TLCs) as presented by Cavadini et al.,^[22] ^{b)}Calculated using the equations in VDI Heat Atlas, Chapter F2, Section 3.^[19]

fraction of solvent at the phase boundary (compare Equation (3)). Moreover, temperature-dependent material parameters like the diffusion coefficient in the gas phase also increase. The results fundamentally confirm the relationships between drying air temperature and resulting film temperature and drying rate described in Section 2. Using the evaluation method described in the Experimental Section, values for the steady-state temperatures and drying rates can be extracted from the convective drying experiments and are listed in Table 1, which will be discussed later.

3.2. Radiation and Forced Convection

In Figure 4, the solvent loading and temperature curves for the process variant “radiation and forced convection” are shown for three different settings of the input power $P_{el, IR}$ of the radiation module. The input power corresponds to the actual power consumption of the module.

The electrode temperature for all settings initially increases to a higher value than the temperature after the application of the coating. After this phase, a steady state is established before a temperature rise indicates the approach to the dry state. The courses of the solvent loadings show fluctuations caused by the impulse of the convection flow on the balance, which persist despite the application of a Savitzky–Golay smoothing. Nevertheless, a linear regression can be used to analyze the data of the solvent loading in the steady state and quantify it with regard to the resulting drying rate. It can be observed that the decrease of the solvent loading is significantly steeper with time and thus the dry state is reached earlier when higher-power inputs are applied. The curves of the corresponding temperature data also show an increase of the mean value in steady state, while the point in time until the steady state is finished is shorter with increasing power. The change in these values can be explained by the increasing heat input by radiation, which is decisive in this process variant. The values for the steady-state temperatures and drying rates can be extracted from the

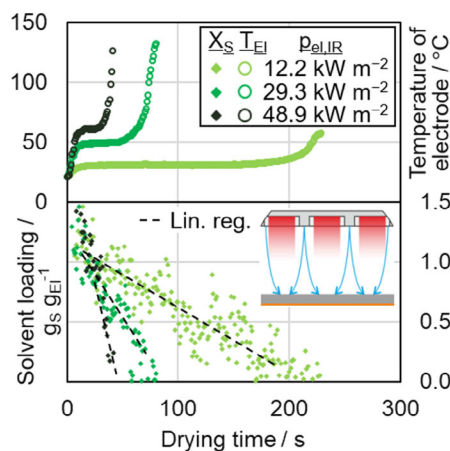


Figure 4. Solvent loading and temperature profiles of electrodes during drying of aqueous-processed anodes: process variant “radiation and forced convection” with variation of the set power of the radiation module at ambient temperature of 21.3 °C, an initial dew point of 8.9 °C, and a mean convective heat transfer coefficient of 36.5 W m⁻² K⁻¹.

described drying experiments and are again listed in Table 1 for a later discussion.

In order to place these results in the overall context, a comparison can first be made with purely convective drying. First of all, the drying curves recorded show qualitatively similar profiles like the profiles from the convective drying trials and only differ quantitatively. Therefore, it can be stated that no difference in the drying mechanism can be detected on the basis of the curves of the process data. Furthermore, the results in Table 1 show that, at comparable or even lower drying rates, significantly higher steady-state temperatures can be achieved with this process variant (e.g., 49.2 °C at 2.05 g m⁻² s⁻¹ with “radiation and forced convection” vs 39.6 °C at 2.80 g m⁻² s⁻¹ with “forced convection”). It can be concluded that this process variant is suitable with regard to the objective of achieving drying at higher possible electrode temperatures compared with the convective process. To ensure that the process meets the requirements for the resulting electrode properties, using adhesion as a representative quality measure, these must also be examined, which is addressed in Section 4. Although high drying rates can be realized at higher temperatures compared with the convective process, the achievable film temperature is still limited. This can be explained by the fact that the air flow exiting between the IR emitters contributes to the cooling of the drying layer and thus counteracts the heating effect of the infrared radiation. Furthermore, the forced convective flow contributes to mass transport in the gas phase and thus increases the drying rate.

Although no economic analysis is made in this study, it should be mentioned that the indicated input powers do not correspond to the emitted power of the infrared emitters, nor the actual energy input at the drying electrode film. The input power in the emitter module is first of all reduced by the conversion of electrical energy in the emitters, while a part of the current is used to operate the fan. Furthermore, a non-negligible amount of energy is bound in the cooling air and then dissipates into the environment. In addition, the absorption coefficient of the electrode, which is between 0.71 and 0.8 for graphite anodes in the relevant wavelength range according to Vedder et al., affects the absorbed radiant power significantly.^[13] Reflection effects on the still wet electrode film can also not be neglected.

3.3. Radiation and Free Convection

In Figure 5, the solvent loading and temperature curves for the process variant “radiation and free convection” are shown for three different settings of the input power $P_{el,IR}$ of the radiation module. To achieve an isolated energy input by radiation, the forced convection flow was completely eliminated using the procedure described in the Experimental Section.

The electrode temperature for all settings initially rises to a higher value, and a steady state is established before a temperature rise indicates the approach to the dry state. The courses of the solvent loadings show no fluctuations, as there is no forced convection flow influencing the scale. Consequently, it can be easily determined that a linear drying slope also occurs in this process variant in the steady state. Again, it can be observed that the decrease of the solvent loading is significantly steeper with time when higher power inputs are applied. The curves of the

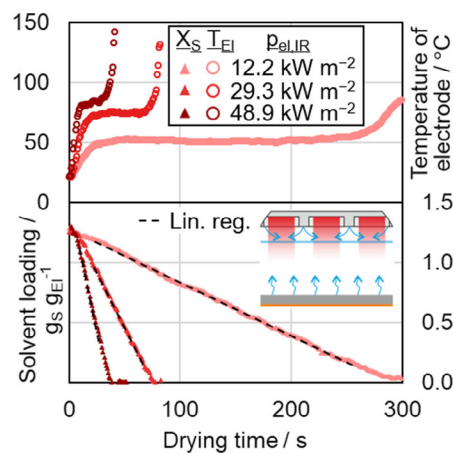


Figure 5. Solvent loading and temperature profiles of electrodes during drying of aqueous-processed anodes: process variant “radiation and free convection” with variation of the set power of the radiation module at ambient temperature of 21.3 °C and an initial dew point of 8.9 °C.

corresponding temperature data also show an increase of the mean value in steady state, while the point in time until the steady state is finished is shorter with increasing power. The change in these values can be explained by the increasing heat input by radiation, which is decisive in this process variant. In addition to the power input, the resulting temperature in the film also has an influence on the solvent transfer. In this process variant, the solvent is not removed with the air introduced via forced convection but rather as a result of the free convection that occurs, depending on the prevailing film temperature. The free convection flow occurs due to the difference in density of the warm and water-loaded air above the drying layer in relation to the ambient air and increases with rising electrode temperature due to the temperature dependence. The characteristic heat transfer coefficient of free convection can be calculated using the equations in the VDI Heat Atlas and lies between 6.0 and 6.9 W m⁻² K⁻¹ for the attempts discussed.^[19] Due to the absence of controlled solvent removal in this process variant, saturation of the ambient air and an increase of the initial dew point, which would influence mass transfer, cannot be ruled out. This must be taken into account for industrial design, but will not be addressed in this publication for the time being. The values for the steady-state temperatures and drying rates can be obtained from the drying tests described and are listed in Table 1, as are the calculated values for the free convection heat transfer coefficients.

In order to place these results in the overall context, a comparison with the other process variants investigated can be conducted. First of all, the drying curves recorded show qualitatively similar profiles like those from the experiments discussed earlier and only differ quantitatively and due to the missing noise of the scale signal. Therefore, it can be stated that no difference in the drying mechanism in the electrode film can be detected on the basis of the curves of the process data. The results show that with comparable drying rates, significantly higher steady-state temperatures can be achieved with the process variant “radiation and free convection” than

in both process variants with forced convection ($74.6\text{ }^{\circ}\text{C}$ at $2.54\text{ g m}^{-2}\text{ s}^{-1}$ with radiation and free convection vs $49.2\text{ }^{\circ}\text{C}$ at $2.05\text{ g m}^{-2}\text{ s}^{-1}$ with radiation and forced convection). It can be concluded that for a given drying rate, the highest film temperatures of the three investigated drying methods can be realized with this process variant. Nevertheless, there is the possibility of further process improvements, for instance, the combination of infrared radiation and tempered, controlled air flow.

As previously mentioned in Section 3.2, no economic analysis is carried out in this study. Even with this process variant, it cannot be assumed that the emitted radiation is completely used for drying. In addition to the efficiency-reducing factors listed, the cooling air with the enthalpy bound therein is completely dissipated into the environment and is not used for drying. At the same time, the glass pane reduces the usable radiator output due to its transmission value of $\approx 90\%$.

3.4. Comparison of the Process Variants

An overview of the measurement data generated in the experiments discussed is shown in Table 1 depending on the process variant and the process parameters.

The values extracted from the process data for the steady-state temperature are also listed in Figure 6 for the various process variants and parameter combinations as a function of the evaluated drying rate.

The tendency already described in the earlier subsections is emphasized: at a comparable drying rate, the steady-state temperature can be significantly increased when using infrared radiation, if the convective heat transfer coefficient is reduced at the same time.

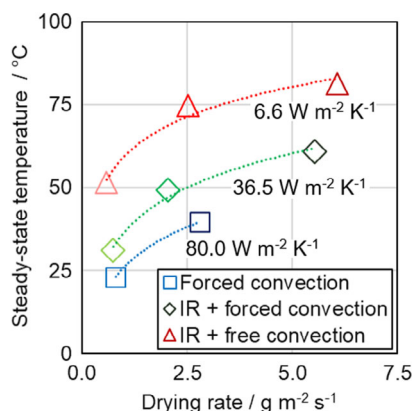


Figure 6. Steady-state temperatures during the drying process as a function of drying rates determined from mass curves during the drying experiments of aqueous-processed anodes for the different process variants. The colors of the data points match the parameter combinations displayed in Figure 3–5. In order to emphasize the tendency of the measured values, they are supplemented by a logarithmic trend curve. The numerical values displayed correspond to the convective heat transfer coefficients within the test series. For the process variant “radiation and free convection,” the mean value of the heat transfer coefficients by free convection from the three parameter combinations investigated is shown.

4. Properties of Dried Electrodes: Adhesion Force

The adhesion force of the electrodes, measured with a 90° peel test, characterizes the influence of the drying process on the electrode properties for the different process variants and parameter settings. The results of these investigations are plotted in Figure 7 as follows: the measured adhesion force, the mean value of three sample strips taken from the electrode area, as a function of the drying rate.

The adhesion within one data series decreases with increasing drying rate. This effect is related to the capillary-driven transport of the binder to the surface of the layer during pore emptying, which is more pronounced at higher drying rates (see Section 1). However, it is noticeable that the absolute values of the adhesion differ between the data series at comparable drying rates. For instance, the adhesion of the process variant “radiation and forced convection” is slightly higher than the adhesion of the process with pure convection drying, while the process variant “radiation and free convection” shows an even more significant increase. In particular, the adhesion is clearly higher at low drying rates, and the adhesion is increased by at least a factor 2 over the entire drying rate range. The combination of the results of the adhesion force measurements and the present drying electrode temperatures (Figure 6) lead to the conclusion that high temperatures correlate with high adhesion forces, when compared at similar resulting drying rates. The fact that high film temperatures, in combination with low convective heat transfer coefficients, can positively affect the binder distribution and electrode adhesion was already discussed in the introduction and is hypothesized in this study. These results confirm the hypothesis in general and verify it for the specific case of drying with energy input by IR radiation.

The adhesion force can also be plotted as a function of the measured steady-state temperatures, which is shown in Figure 8.

The adhesion force decreases with increasing film temperature, which corresponds to an increasing drying rate if the

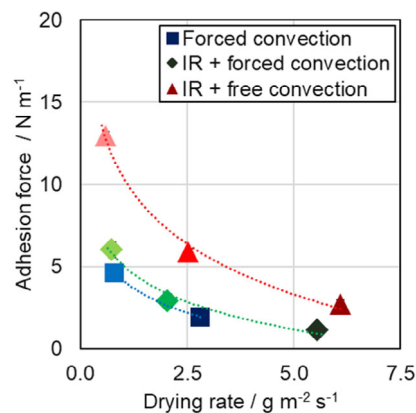


Figure 7. Adhesive forces of dried electrodes as a function of drying rates determined from mass curves during the drying experiments of aqueous-processed anodes for the different process variants. The colors of the data points match the parameter combinations displayed in Figure 3–5. In order to emphasize the tendency of the measured values, they are supplemented by a logarithmic trend curve.

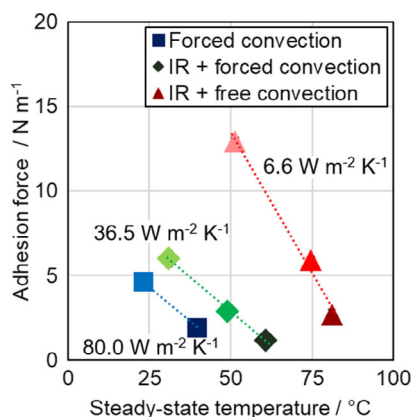


Figure 8. Adhesion forces of dried electrodes as a function of the steady-state temperatures determined from the temperature curves during the drying experiments of aqueous-processed anodes for the different process variants. The colors of the data points match the parameter combinations displayed in Figure 3–5. In order to emphasize the tendency of the measured values, they are supplemented by a linear trend curve. The numerical values displayed correspond to the convective heat transfer coefficients within the test series. For the process variant “radiation and free convection,” the mean value of the heat transfer coefficients by free convection from the three parameter combinations investigated is shown.

boundary conditions remain constant apart from the selected air temperature or radiation power. The advantage of the infrared radiation drying process in terms of adhesion can also be clearly seen in this diagram: High temperatures can only be reached with low convective heat transfer coefficients and heat input by radiation, which is the combination that leads to high adhesion values. While the data points in Figure 7 can be approximated with a logarithmic curve, the trend lines in the data series in Figure 8 are nearly linear. This can be explained by the relationship between the two process values of interest discussed here: The drying rate is a logarithmic function of the molar fraction of solvent at the phase boundary of the drying electrode which is dependent on the prevailing film temperature (compare Equation (3) and (4)).

To illustrate the importance of the film temperature in the process in relation to the drying rate, the adhesion values are plotted as a function of the ratio of steady-state temperature to drying rate in Figure 9.

The diagram shows that the measured values are approximately on a line. The key statement of the diagram confirms that an increasing ratio of drying temperature in the steady state to drying rate leads to a high adhesion force. It is remarkable that the slope describes adhesion force data regardless of the type of process carried out, leading to the conclusion that the development of the binder distribution and consequently the adhesive force is independent of the type and manner of energy input but only on the drying rates and film temperatures reached during the process. Nevertheless, it must be mentioned that the results are only valid for aqueous-processed graphite anodes with the specified formulation used, a dry area weight of 130 g m^{-2} , and the three discussed process variants. However, for upscaling and industrial application, the removal of solvent from ambient air in the drying environment must be considered and further

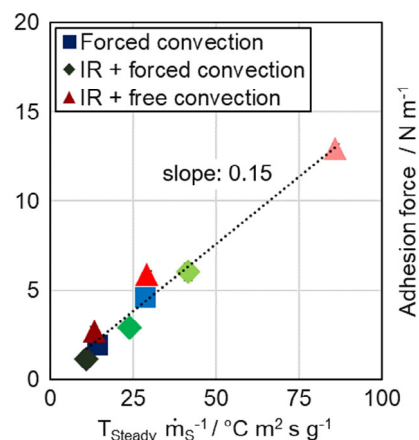


Figure 9. Adhesion forces as a function of the ratio of steady-state temperature to drying rate for aqueous-processed anodes dried with different process variants. The colors of the data points match the parameter combinations displayed in Figure 3–5. To illustrate the tendency of the measured values, they are supplemented by a linear trend curve.

electrochemical studies must be conducted on the performance of the infrared-processed battery electrodes.

5. Conclusion

The investigation of three drying configurations demonstrates the influence of convective and radiation-based process parameters on the electrode drying process and the resulting electrode properties. In detail, the influence on the film temperature of drying electrodes as well as the drying speed and the adhesion of these electrodes is discussed.

Theoretical Considerations: In case of drying with forced convection, the process parameters and limitations with regard to achievable steady-state temperatures and drying rates as a function of heat transfer coefficient, dryer temperature, and dew point are shown analytically. The same methodology was used to demonstrate the suitability of heat input by radiation under the absence of forced convection. The observations show that the application of radiation in the drying process can be beneficial to selectively control drying rate and film temperature. In particular, it is shown that higher film temperatures can be achieved with infrared radiation than with purely convective drying at comparable drying speeds. In combination with the hypothesis that high film temperatures during drying can have a positive influence on the electrode properties, the theoretically demonstrated effects provide the motivation for the experimental approach in which these are verified on the one hand and extended by determining the electrode quality on the other.

Experimental Approach: The process variants “forced convection,” “infrared radiation with forced convection,” as well as “infrared radiation with free convection” were investigated by means of different parameter combinations in batch drying tests for aqueous-processed anodes with an area weight of 130 g m^{-2} , corresponding to a theoretical electrode capacity of $\approx 4.65 \text{ mAh cm}^{-2}$. The electrode temperatures and drying rates resulting from measured mass and temperature profiles, along

with the subsequent electrode characterization, allow clear conclusions to be drawn. The results confirm that the highest electrode temperatures can be achieved with the application of pure infrared radiation and that the ratio of temperature to drying rate is highest with this process variant, which was expected on the basis of the theoretical considerations. Moreover, the experiments confirm the positive effect of high temperatures resulting from heat input with radiation on the electrode properties. This is demonstrated by adhesion force measurements, which show that IR-dried electrodes have significantly better adhesion at comparable drying rates, indicating the presence of a binder distribution and condition that is beneficial to good electrode adhesion. As a result, electrodes can be produced at higher throughput rates with the process variant presented, whereby the drying rate at which a critical deterioration of the product properties, that is, adhesion, occurs is reached later than with the conventional process.

For upscaling and industrial application, the removal of solvent from the ambient air in the drying environment must be considered and further investigations on the electrochemical properties regarding the performance of the battery electrodes processed with infrared radiation must be carried out. Nevertheless, the results presented position the drying process with heat input by infrared radiation promisingly in the application for electrode production.

6. Experimental Section

Formulation and Slurry Preparation: For slurry preparation, CMC (Sunrose MAC500LC, Nippon Paper Industries Co., Ltd., Japan) was dissolved in water at ambient temperature in a laboratory stirrer for 1 h at 500 rpm. Graphite particles (SMGA, Hitachi Chemical Co. Ltd., Japan) and carbon black (Super C65, Timcal SA, Switzerland) were mixed in a dry mixing step for 10 min at 300 rpm in a dissolver mixer (Dispermat CN10, VMA Gretzmann GmbH Verfahrenstechnik, Germany). Solids were added to the CMC water solution in three thickening steps while stirring the mixture at 500 rpm. While the temperature of the vessel was temperature-controlled by cooling water, degassing was executed and the slurry was dispersed at 1500 rpm for 45 min. In a last step, SBR binder (Zeon Europe GmbH, Japan) was added and the dispersion was mixed at 500 rpm for 10 min. The resulting mass composition of the components is listed in **Table 2**.

Coating: For the coating step, 10 μm -thick copper foil (Civen Metal Material Co. Ltd., China) was used as a substrate. To realize a homogeneous surface in crossweb direction and guarantee defined coating and drying conditions, the foil was fixed into a tensioned frame and placed on a flat coating plate equipped with a vacuum groove suction. A doctor blade (UA2000.100, Proceq SA, Switzerland) was used to apply films of defined thickness and geometry. For coating, the doctor blade was moved by a linear actuator at a speed of 50 mm s^{-1} , while the coating gap was adjusted to 265 μm to achieve a dry area weight of $\approx 130 \text{ g m}^{-2}$. In order to obtain the same electrode geometry in each experiment, a 20 μm -thick PET stencil with a cut-out area of 90 by 90 mm was used during the coating process. The stencil was removed after the coating prior to drying.

Drying: Following coating, the electrodes were dried with three different process variants. At the beginning of the experiments, the ambient temperature was 21.3 $^{\circ}\text{C}$ and the relative humidity was 46.3%, which corresponded to an initial dew point of 8.9 $^{\circ}\text{C}$. For each drying scenario presented in Section 2, one exemplary single measurement is shown. For the purely convective drying process, a batch dryer with impingement jets with a homogeneous distribution of heat transfer coefficients and solvent removal was used.^[22] For these experiments, an average heat transfer coefficient of 80 $\text{W m}^{-2} \text{K}^{-1}$ was set, while the drying air temperature was chosen between 45 and 120 $^{\circ}\text{C}$. Drying was performed at constant

Table 2. Composition of the dry electrode and the electrode slurry.

Component	Dry mass fraction [wt%]	Wet mass fraction [wt%]
Graphite	93.00	39.99
Carbon black	1.40	0.60
CMC	1.87	0.80
SBR	3.73	1.60
Water	–	57.00

parameters until the coating was sufficiently dried, indicated by the temperature rising toward the adjusted air temperature.

For drying with energy input by infrared radiation and forced convection, a commercially available IR module consisting of three infrared emitters divided and surrounded by a reflective housing and air flow slots was applied. The module covered an area of 124 by 330 mm with a maximum power of 3.3 kW at a wavelength around 1 μm . Its ventilation slots were supplied by air, which was drawn in at ambient temperature by an integrated axial fan. The flowing air served to cool the reflector surface as well as the IR emitters. As the cooling air was released below the module, an influence on the drying process was inevitable. The module is shown schematically in **Figure 10**.

In the drying experiments, the input power $P_{\text{el,IR}}$ of the module was varied between 500, 1200, and 2000 W, which corresponded to an area-related input power $P_{\text{el,IR}}$ of 12.2, 29.3, and 48.9 kW m^{-2} , respectively. The module was positioned at a distance of 120 mm above the coating, while the air flow could not be adjusted due to the design of the module. For drying, the module remained switched on at constant power setting until the coating was sufficiently dried, as indicated by a rapid temperature increase. The drying module was switched off when the measured temperature reached about 130 $^{\circ}\text{C}$.

For drying with energy input by infrared radiation without forced convection, the same configuration and procedure was used, with the exception that an IR-transmissive panel was installed underneath the module. The glass ceramic panel-type MERAX (Mennes GmbH, Germany) with 3 mm thickness had a transmission of about 90% in the relevant wavelength range (from 750 to 2500 nm), while the air exiting the radiation module was deflected, allowing an isolated energy input by infrared radiation during drying. The cooling function of the IR module remained unaffected.

Measurement Data Acquisition: Temperature Curves and Drying Rate: The drying progress was determined on the basis of mass and temperature curves. After slurries were applied to a defined surface as described earlier, a thermocouple was attached centered beneath the substrate. Due to the high thermal conductivity of copper and the low thickness of the electrode layer, the temperature at this point was considered to be a representative electrode temperature. As the electrode-carrying tensioned frame was mounted on a rack placed on a scale-type MC1 LC12005 (Sartorius AG, Germany) during the experiments, mass curves could be analyzed (compare **Figure 11**).

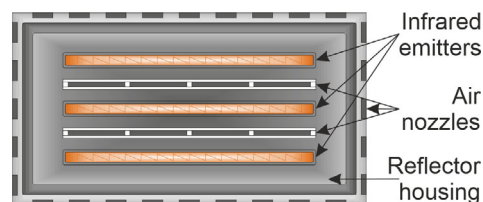


Figure 10. Schematic illustration of the configuration of the infrared module used.

The mass profiles $M_{EI}(t)$ were converted into curves of solvent loading $X_S(t)$ for reasons of comparability with Equation (5).

$$X_S(t) = \frac{M_S(t)}{M_{EI, dry}} = \frac{M_{EI}(t) - M_{EI, dry}}{M_{EI, dry}} \quad (5)$$

Here, $M_S(t)$ corresponds to the mass of the solvent. For this procedure, the tensioned frame with a mounted current collector was weighed separately before each experiment and after, then containing the dried electrode coating, to determine the dry electrode coating mass $M_{EI, dry}$. The slope of a linear regression considering the measured values in the steady state divided by the electrode area determines the drying rate. The steady-state temperature was obtained by averaging the temperatures of the period in which an almost constant temperature was present. The described procedure is shown in **Figure 12** for one example.

The investigations carried out with the infrared radiator without the use of the convection-flow dissipating plane provided measurement data for the mass curves, which in some cases showed strong fluctuations caused by the impulse of the convection current on the balance. For this reason, the measurement data for mass was processed using a second-order Savitzky-Golay smoothing (five fixed points).

Adhesion Measurement: Adhesion force was measured using a universal testing machine type AMETEK LS1 (Lloyd Instruments Ltd., UK) with a 90° peeling device and a 10 N load cell. Specimens of 28 mm width were tested, and cut perpendicular to the coating direction, using three specimens per electrode. The mean value and the standard deviation were determined.

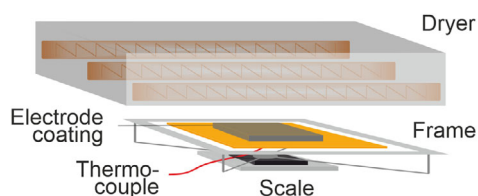


Figure 11. Experimental setup for the drying experiments: the coated, drying anode layer mounted in a tensioned frame is located in a defined distance below the drying module during drying. To control the temperature curve, a thermocouple is fixed below the copper foil with thermal conductive paste while the mass is logged by a precision scale.

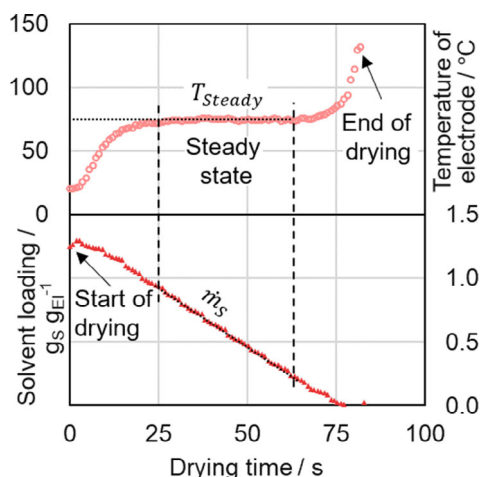


Figure 12. Illustration of the determination of the steady-state temperature and drying rate using the example of IR drying of an aqueous-processed electrode at an area-related power input of the IR module of 29.3 kW m^{-2} .

Supporting Information

Supporting Information is available from the Wiley Online Library or from the author.

Acknowledgements

The authors would like to thank the students Julian Borho and Rafael Manrique Gutierrez as well as the research associates Kevin Ly and Jonas Mohacsi for their support. The authors would like to acknowledge financial support of the Federal ministry of Education and Research (BMBF) via the ProZell cluster-project “Epic” (Grant number: 03XP0295A). This work contributes to the research performed at Center for Electrochemical Energy Storage Ulm-Karlsruhe (CELEST).

Open Access funding enabled and organized by Projekt DEAL.

Conflict of Interest

The authors declare no conflict of interest.

Data Availability Statement

The data that support the findings of this study are available from the corresponding author upon reasonable request.

Keywords

adhesions, binder migrations, drying, lithium-ion battery electrodes, near infrared

Received: July 18, 2022

Revised: August 23, 2022

Published online:

- [1] L. Mauler, F. Duffner, J. Leker, *Appl. Energy* **2021**, *286*, 116499.
- [2] R. Diehm, M. Müller, D. Burger, J. Kumberg, S. Spiegel, W. Bauer, P. Scharfer, W. Schabel, *Energy Technol.* **2020**, *8*, 2000259.
- [3] D. L. Wood, J. D. Quass, J. Li, S. Ahmed, D. Ventola, C. Daniel, *Dry. Technol.* **2018**, *36*, 234.
- [4] M. Baunach, S. Jaiser, S. Schmelzle, H. Nirschl, P. Scharfer, W. Schabel, *Dry. Technol.* **2016**, *34*, 462.
- [5] S. Jaiser, N. Sanchez Salach, M. Baunach, P. Scharfer, W. Schabel, *Dry. Technol.* **2017**, *35*, 1807.
- [6] S. Jaiser, M. Müller, M. Baunach, W. Bauer, P. Scharfer, W. Schabel, *J. Power Sources* **2016**, *318*, 210.
- [7] M. Müller, L. Pfaffmann, S. Jaiser, M. Baunach, V. Trouillet, F. Scheiba, P. Scharfer, W. Schabel, W. Bauer, *J. Power Sources* **2017**, *340*, 1.
- [8] J. Klemens, L. Schneider, E. C. Herbst, N. Bohn, M. Müller, W. Bauer, P. Scharfer, W. Schabel, *Energy Technol.* **2022**, *10*, 2100985.
- [9] J. Kumberg, M. Müller, R. Diehm, S. Spiegel, C. Wachsmann, W. Bauer, P. Scharfer, W. Schabel, *Energy Technol.* **2019**, *7*, 1900722.
- [10] B. Westphal, H. Bockholt, T. Gunther, W. Haselrieder, A. Kwade, *ECS Trans.* **2015**, *64*, 57.
- [11] S. Jaiser, J. Kumberg, J. Klaver, J. L. Urai, W. Schabel, J. Schmatz, P. Scharfer, *J. Power Sources* **2017**, *345*, 97.
- [12] *Handbook Of Industrial Drying* (Ed: A. S. Mujumdar), CRC Press, Boca Raton, FL **2015**.

- [13] C. Vedder, D. Hawelka, M. Wolter, D. Leiva, J. Stollenwerk, K. Wissenbach, in *Int. Congress on Applications of Lasers & Electro-Optics*, Laser Institute of America, Orlando, FL **2016**, N501.
- [14] X. F. Wu, X. J. Li, X. Z. Bei, *MSF* **2020**, 1003, 260.
- [15] S. Y. Kim, S. Rhee, *Int. J. Electrochem. Sci.* **2011**, 6, 5462.
- [16] W. Pfleging, *Nanophotonics* **2018**, 7, 549.
- [17] T. Günther, N. Billot, J. Schuster, J. Schnell, F. B. Spingler, H. A. Gasteiger, *AMR* **2016**, 1140, 304.
- [18] E. Wiegmann, A. Kwade, W. Haselrieder, *Energy Technol.* **2022**, 10, 2200020.
- [19] VDI Heat Atlas, Springer Vieweg, Berlin, Heidelberg, **2013**.
- [20] E.-U. Schlünder, *Dry. Technol.* **2004**, 22, 1517.
- [21] J. Kumberg, M. Baunach, J. C. Eser, A. Altvater, P. Scharfer, W. Schabel, *Energy Technol.* **2021**, 9, 2100013.
- [22] P. Cavadini, P. Scharfer, W. Schabel, in *Proc. of the 15th Int. Heat Transfer Conf.*, Begellhouse, CT **2014**.